UNIVERSITY OF CALIFORNIA

Los Angeles

Growth and Characterization of Zr and ZrC Thin Films on Al_2O_3(0001)

A thesis submitted in partial satisfaction

of the requirements of the degree Master of Science

in Materials Science and Engineering

by

Joshua Paul Fankhauser

2016

ABSTRACT OF THESIS

Growth and Characterization of Zr and ZrC Thin Films on Al_2O_3(0001)

by

Joshua Fankhauser

Master of Science in Materials Science and Engineering

University of California, Los Angeles, 2016

Professor Suneel Kodambaka, Chair

I report the growth of epitaxial Zr(0 0 0 1) and ZrC(1 1 1) thin films on Al_2O_3(0 0 0 1) via dc magnetron sputtering in an ultra-high vacuum deposition system equipped with facilities for chemical vapor deposition, low-energy electron diffraction, and Auger electron spectroscopy. Zr layers with a nominal thickness up to 270 nm are deposited at a rate of ~0.07 nm/s in 10 mTorr Ar (99.999%) atmosphere. ZrC layers with a nominal thickness up to 110 nm are deposited at a rate of ~0.06 nm/s in 10 mTorr atmosphere composed of 1 mTorr C_2H_4 (99.999%) and 9 mTorr

Ar. As part of my thesis work, I investigate the effect of substrate temperature during sputter-deposition on the composition and crystallinity of the Zr and ZrC films. The as-deposited films are characterized *in situ* using Auger electron spectroscopy and low energy electron diffraction and *ex situ* using x-ray diffraction, transmission electron microscopy, energy dispersive x-ray spectroscopy, and x-ray photoelectron spectroscopy. I deposited Zr thin films at temperatures between 600 °C and 900 °C. My x-ray diffraction studies reveal that increasing the substrate temperature during sputter-deposition of Zr leads to the growth of polycrystalline hexagonal close-packed structure Zr films. Cross-sectional transmission electron microscopy images reveal columnar growth and the formation of an interfacial layer, whose thickness increased with increasing temperature. Energy dispersive x-ray spectra obtained from this region reveal the presence of both Zr and Al. I attribute the formation of this interfacial layer to plasma-induced substrate decomposition followed by interdiffusion of Al and Zr at the film-substrate interface during sputtering. I deposited ZrC layers at temperatures between 800 °C and 1400°C. X-ray diffraction data acquired from my samples indicate that the crystallinity improves with increasing temperature. X-ray photoelectron spectra reveal that all of my films contain excess carbon, whose content decreases with increasing temperature. Based upon my results, I identify optimal growth temperatures for obtaining single-crystalline and epitaxial Zr and ZrC layers.

The thesis of Joshua Paul Fankhauser is approved.

Jenn-Ming Yang

Mark Goorsky

Suneel Kodambaka, Committee Chair

University of California, Los Angeles

2016

Table of Contents

Acknowledgements

I would like to thank Prof. Kodambaka for his guidance and express my appreciation for his help in completing these experiments. In addition, I would like to thank Dr. Abbas Ebnonnasir for his patience and assistance with teaching me the principles of ultra-high vacuum (UHV). Without his help, I would never have been able to operate and understand the capabilities of a UHV system. I cannot thank Dian Yu enough for all of her time spent performing transmission electron microscopy, without which I would not have completed this thesis. In addition, I would like to thank Prof. Goorsky and Chao Li for their assistance with the acquisition and analysis of my x-ray diffraction data. My lab group of Abbas Ebnonnasir, Pedro Arias, Denisa Vlasache, Masaki Sato, and Taichi Nakao, kept me going through my entire time at UCLA and made every day interesting. I would like to thank my better half Kellie Brown for all the time and support she has given me over the past six years. Finally, I would like to thank my family for their support in my pursuit of this M.S. degree and throughout my life.

Chapter 1: Introduction

1.1 Transition Metal Carbides

The aerospace industry has long been reliant on coating technologies. Spacecraft, rockets, and hypersonic vehicles all operate under extreme environments experiencing high temperatures (>2200 °C), drastic thermal cycling, and both neutral and oxidizing atmospheres. In order to survive such environments, materials are selected with desirable properties such as oxidation resistance, a low vapor pressure at operating temperatures, good mechanical properties, and chemical stability.[1] One class of materials is favored as a potential candidate for these coatings, transition-metal carbides (TMC). This class of materials has some of the highest melting temperatures and generally exhibit high strengths and hardnesses, as well as good corrosion resistances.[2] One such TMC is ZrC, which has many of these desirable characteristics as will be described below.

1.2 Properties of Zirconium and Zirconium Carbide

The parent element in ZrC is the group IVB transition-metal Zr. Elemental Zr exhibits a hexagonal close-packed (hcp) crystal structure at room temperature with bulk in-plane (a) and out-of-plane (c) lattice parameters of 0.3233 nm and 0.5149 nm, respectively.[3] At a temperature T > 863 °C,[4] Zr undergoes a phase transition from hcp to body-centered cubic (bcc) and retains the same structure until its melting point (1852 °C).[5] Pure Zr has a tensile strength of 150 – 270 MPa and an elastic modulus of 72 GPa and is considered to be one of the more ductile metals due to the fact that it deforms on three independent slip planes and

multiple twinning planes.[5, 6] In addition, Zr also has a low absorption cross section of 0.18 ± 0.02 barns for thermal neutrons.[6]

As a transition-metal refractory carbide, ZrC is known primarily for its physical properties such as: high hardness (25-35 GPa), high melting temperature of ~3500 °C, chemical inertness to strong aqueous acids and bases, metal-like resistivity (5×10^{-7} Ω•m), and relatively low work function (4.0 eV) compared to materials such as Si and Mo.[7-11] ZrC exhibits NaCl structure with a bulk lattice parameter of 0.46976 nm and typically contains 0.5-2 at.% Hf impurities.[12]

1.3 Applications of Zirconium

Zr is primarily used in nuclear reactors as a structural material due to its high corrosion resistance to acids and bases, good mechanical properties, and low absorption cross section.[6, 13] Zr is also used as a fuse, as a primer, as a getter in vacuum tubes, in chemical processing plants,[5] and as an alloying element.[14] Zirconium based compounds such as zircon ($ZrSiO_4$) are used as a refractory material in glasses and steels, ZrC and ZrN as hard protective layers on cutting tools, and ZrB_2 as thermally-resistive hard coatings in hypersonic vehicles.[15, 16] Metallic Zr thin films are used in multi-layer nuclear fuel particles, as high-strength and diffusion-barrier layers,[17] as corrosion resistant coatings on both high carbon steel cutting tool tips,[18] and on "First Mirrors", used for optical diagnosis of the nuclear fusion process.[19]

1.4 Applications of Zirconium Carbide

ZrC is commonly used in the aerospace industry, for example in hypersonic vehicles, due to its thermochemical and thermomechanical stabilities in extreme operational

environments.[20] ZrC thin films are considered as potential replacements for SiC as the main pressure barrier in multi-layer nuclear fuel particles due to the fact that ZrC does not undergo any phase transitions, has very little reaction with Pd, and has good fission product retention capability.[10] The tribological properties of ZrC are attractive for a variety of applications. For example, ZrC coatings can be used on sliding electrical contacts due to their high hardness and conductivity, in micro-electromechanical devices, in circuit breakers, and in motor vehicle starters.[21]

1.5 Growth of Zirconium

Zirconium thin films are deposited using a few different methods (outlined below) all within the category of physical vapor deposition (PVD). Zr is highly reactive and readily forms compounds upon exposure to air. Therefore, pure Zr films are best grown in a high or an ultra-high vacuum (UHV) chamber and inert atmospheres.

1.5.1 Magnetron Sputtering

One approach to the growth of Zr thin films is to use magnetron sputtering. In this method a metallic target is placed on a magnetron in an inert gaseous atmosphere. The magnetron generates plasma at the surface of the target and the gas ions present in the discharge knock off the target material, some of which is collected on the substrate surface. For sputter-deposition of zirconium thin films, a pure Zr target is used. The plasma is generated with an argon atmosphere at pressures typically between 1 and 10 mTorr. By controlling the argon flow, target power, deposition time, and substrate temperature, the film thickness and deposition rate can be tailored. This method allows for a wide range of film thicknesses from

tens of nanometers to a few micrometers. Using magnetron sputtering, Zr thin films have been deposited on high carbon steel, SiC, and Al_2O_3. [17, 18, 22]

1.5.2 Pulsed Laser Deposition

An alternate technique to the deposition of Zr thin films is to use pulsed laser deposition (PLD). In this method, a nanosecond laser pulse strikes a pure Zr target causing the ablation of target material, some of which is deposited on the substrate surface. The laser is typically operated at a wavelength of 248 nm and both the duration of the laser pulse and the incident angle are dependent on the system and specific application. In order to avoid uneven wear on the Zr target, the target can be rotated throughout the deposition. PLD of Zr thin films have been reported on Al_2O_3, GaN/Al_2O_3, and Si substrates.[19, 23, 24]

1.6 Growth of Zirconium Carbide

ZrC can be deposited via both chemical vapor deposition (CVD) and PVD, preferably in UHV. Within the scope of PVD, films can be deposited using premade ZrC compound sources or using a combination of Zr and C precursors. Methods of PVD include thermal evaporation, PLD, and magnetron sputtering.

1.6.1 Chemical Vapor Deposition

Two different approaches for CVD of ZrC have been reported in the literature. In one method, zirconium tetrachloride ($ZrCl_4$) and methane (CH_4) are used as precursors in fluidized-bed CVD. In this technique, the substrates are loaded into a reaction chamber and $ZrCl_4$ powder is vaporized in a separate apparatus, where Ar is used as a carrier gas. CH_4 is then flowed into the reaction chamber with H_2 as a dilution gas. Fluidized-bed CVD is capable of deposition on three-dimensional (3D) surfaces, such as spherical particles.[10] In the

second method, aerosol-assisted metalorganic CVD uses $C_{20}H_{44}Zr$ solutions as a ZrC source. The precursor is made into an aerosol and H_2 is used as a carrier gas. This approach has produced amorphous ZrC thin films when deposited at low growth rates and substrate temperatures of 400 to 600 °C.[9]

1.6.2 Thermal Evaporation

ZrC can also be deposited via thermal evaporation. In this process, an evaporator resistively heats a ZrC compound source to near its melting temperature (~3500 °C) which creates a zone melted ZrC crystal. The evaporator is located near the substrate such that the evaporated material will be deposited on the substrate. This method has been used to grow ZrC thin films on both W and Mo substrates.[11, 25]

1.6.3 Pulsed Laser Deposition

ZrC thin films have also been synthesized via PLD. A nanosecond laser pulse, typically set at a wavelength of 248 nm, ablates a ZrC target in order to deposit material onto the substrate. The duration of the laser pulses, the incident angle, and the substrate temperatures may all be set to influence crystallinity as well as thickness of the resulting films. Film compositions can be tailored if the depositions take place in a carbon atmosphere (C_2H_2 or CH_4).[26, 27]

1.6.4 Magnetron Sputtering

One of the most common forms of deposition is that of magnetron sputtering. First, an elementally pure Zr target can be combined with a gaseous carbon source in reactive magnetron sputtering. As with the other deposition methods, this process is done in either a high vacuum or a UHV system. The deposition atmosphere is typically a combination of high purity Ar and a carbon source (C_2H_2, CH_4, or C_2H_4). Magnetron power, substrate temperature, Ar and carbon source flow rates, and relative partial pressures, and deposition time can be set

independently in order to influence the growth rate, surface roughness, crystallinity, and composition of the ZrC films.[21, 28, 29]

Rather than using a reactive gas atmosphere, ZrC thin films can also be deposited directly via sputtering of a zirconium carbide target or co-sputtering of zirconium and carbon targets a pure Ar environment. Similar to reactive sputter deposition, magnetron power, substrate temperature, and Ar flow rate can be set to tailor the film thickness, composition, and crystallinity.[30, 31]

Chapter 2: Experimental

2.1 Zr Thin Film Deposition

All of my Zr films are grown in a custom-designed ultra-high vacuum (UHV) deposition system with a base pressure of 2.0×10^{-10} Torr achieved through the use of a combination of 685 l/s turbomolecular pump and 60 l/s ion pump. The system is equipped with a load-lock chamber, a dc magnetron (Kurt J. Lesker), residual gas analyzer (Pfeifer Vacuum), fully UHV-compatible reverse-view LEED/AES assembly (LK Technologies), and multiple ports for dosing gases through UHV leak valves. The substrates are single-side polished 2×10 mm^2 rectangular pieces of Al_2O_3(0 0 0 1) cut out of 10×10 mm^2 single-crystals (from MTI) using a diamond wheel saw. The substrates are cleaned via sonication sequentially in acetone and isopropyl alcohol, blown dry with compressed nitrogen, sonicated in deionized water, and baked in air at 200 °C in an oven for 45 min. The samples are then mounted on a heating stage made of two plates of pyrolytic boron nitride; the stage is capable of achieving temperatures up to 1400 °C through direct current heating of a 0.13-mm-thick, 8×14 mm^2, molybdenum foil placed between the two plates. The sample-heater assembly is introduced into the UHV deposition system through the load-lock chamber. Prior to sample transfer, the load-lock chamber is evacuated using a 50 l/s turbomolecular pump until a pressure of $\sim 10^{-8}$ Torr is achieved. This process typically requires up to 45 minutes. Upon transferring the sample-stage to the main chamber, the sample is degassed and held at ~1000 °C until the chamber pressure is below 6.0×10^{-9} Torr. Temperature is measured using an IMPAC IS 8-GS pyrometer positioned outside of the vacuum chamber approximately 40 cm from the sample. The orientation of the pyrometer with respect to the sample is set to 90°. All of my

temperature measurements are obtained from bare Al_2O_3 substrates mounted on Mo foil prior to film depositions. The emissivity of Mo[32] is assumed to be 0.13 ± 0.02. At any given temperature, I measure a maximum variation of $\pm$ 100 K across the substrate. These values do not account for plasma heating during depositions.

Prior to Zr film deposition, the sample is cooled from 1000 °C to the deposition temperature (as measured on bare Al_2O_3 on Mo foil) and the ion pump is switched off because my deposition pressures (mTorr) are above its safe operational limits of 10^{-7} Torr. At the growth temperature, the chamber is at or below a pressure of 6×10^{-9}. (Disabling the pump, however, has little effect on the chamber pressure, which increases by ~2×10^{-10} Torr.) All the depositions are carried out in 10 mTorr Ar (99.999% pure) atmosphere with the Ar introduced through an UHV leak valve. The magnetron is equipped with a 50-mm-diameter × 3-mm-thick Zr (99.1% pure with ~0.8 at. % Hf) target (ACI Alloys, Inc.). The target is located ~30 cm above the substrate surface. All of my Zr thin films are grown using a constant power of 50 W. The corresponding voltage measured during my depositions is 210 V. The deposition time is 60 minutes. The substrate temperature (T_s) is the only variable in my experiments, which I changed in increments of 50 K and grew samples at T_s between 600 °C and 900 °C. This procedure yields Zr films with a nominal thickness up to ~270 nm, as measured from cross-sectional TEM images. (The actual film thickness will be higher as this value does not include the Zr present within the interface.) Based upon this data, I estimate a deposition rate of ~0.07 nm/s. After deposition, the chamber is evacuated and the sample is cooled to room temperature.

2.2 ZrC Thin Film Deposition

ZrC thin films are sputter-deposited on Al_2O_3(0 0 0 1) following a procedure similar to that described above for the growth of Zr thin films. The Al_2O_3(0 0 0 1) samples are cut, cleaned, and loaded into the UHV load-lock chamber where they remain until the chamber is pumped to ~10^{-8} Torr. They are then loaded into the main chamber, where they are degassed at 1400 °C prior to deposition.

Prior to introducing the gases, I decrease the speed of the turbo molecular pump from 46,000 rpm to 37,000 rpm. The decreased speed ensures steady and reliable pressure readings for each component of the deposition atmosphere. In all of these experiments, the gases are introduced through UHV leak valves. In order to create the desired reactive deposition atmosphere, the chamber is initially filled to a pressure of 1 mTorr with ethylene (99.999% pure), and 9 mTorr of Ar (99.999% pure) is then added such that the total pressure is increased to 10 mTorr. I change the substrate temperature in increments of 100 K from 800 to 1400 °C. All of my ZrC thin films were grown using a power of 14 $\pm$ 2 W (200 V) for 30 minutes. The resulting film thicknesses are found to vary with T_s. At the end of deposition, the chamber is evacuated and the sample is cooled to room temperature.

2.3 Characterization

I begin characterization of the as-deposited ZrC samples after the base pressure of the chamber has improved to less than 6.0×10^{-9} Torr. The surfaces of my as-deposited films are first characterized *in situ* to determine their crystallinity and composition. The samples are then removed from vacuum and characterized *ex situ* using a variety of techniques to

determine the film crystallinity, morphology, thickness, composition, and lattice parameters. All of these methods are described below.

2.3.1 Low Energy Electron Diffraction & Auger Electron Spectroscopy

I used *in situ* low energy electron diffraction (LEED) and Auger electron spectroscopy (AES) for the surface characterization of Zr thin films deposited on Al_2O_3(0 0 0 1) substrates. The LEED/AES system is equipped with 4-grid LEED optics and a phosphor viewing screen. It has a low-profile electron gun capable of electron beam currents up to 2 μA at 100 eV and, for Auger operation, up to 50 μA. The AES data is obtained using a 1 keV primary beam at kinetic energies between 130 and 550 eV. The spectra are acquired with a step size of 0.165 eV and a dwell time of 0.2 s. Surface structure is determined using LEED with a screen voltage of 4 kV, a Can aperture voltage of 14 V, and at incident electron energies between 60 and 250 eV.

2.3.2 X-ray Photoelectron Spectroscopy

Composition of ZrC/Al_2O_3(0 0 0 1) thin films is determined using x-ray photoelectron spectroscopy (XPS). X-ray photoelectron spectra are obtained using a Kratos Analytical AXIS Ultra DLD at energies between 0 and 1200 eV with a pass energy of 160 eV, a step size of 1.0 eV, and an acquisition time of 0.1 s/step. After loading the samples into the XPS system, the surfaces are cleaned by sputter-etching using Ar^+ for two minutes. Higher resolution scans are also acquired around the C 1s peak (284.8 eV) over a range of 271 – 296 eV with a step size of 0.1 eV and a dwell time of 0.45 s/step to identify the carbon bonding states. The data is acquired twice and integrated to improve the signal to noise ratio.

2.3.3 X-ray Diffraction

X-ray diffraction (XRD) 2θ-ω spectra along with high-resolution symmetric and asymmetric reciprocal space maps (RSMs) are obtained in order to determine the crystallinity and lattice parameters of both Zr and ZrC thin films. 2θ-ω scans are obtained using Bede D1 powder diffractometer in order to determine the crystallinity of the Zr films. The diffractometer is equipped with a sealed copper x-ray tube source and a MaxFlux specular mirror to produce a parallel beam. Single-crystalline samples are analyzed using a Bede D1 high-resolution diffractometer. This diffractometer is identical to the powder diffractometer with the exception of an additional two bounce channel-cut (2 2 0) Si collimator crystal, which generates a monochromatic incident beam specific to the Cu $K\alpha_1$ wavelength (0.154056 nm).

For 2θ-ω measurements, samples are mounted vertically on a Si(0 0 1) wafer to eliminate any background signal from the diffractometer stage. First, the detector and x-ray optics are aligned to achieve maximum straight-through intensity. Then, the sample and stage are calibrated with respect to ω, φ (out-of-plane rotation perpendicular to ω), and χ (in-plane rotation) about the Al_2O_3(0 0 0 6) peak, 2θ = 41.68°. For the Zr films, 2θ-ω scans between 15 and 98° are acquired using double-axis diffraction with a step size of 0.05° and a dwell time of 1 s. High-resolution symmetric RSMs are obtained over a range of 12° in ω-2θ with a step size of 200” and 4° in ω with a step size of 250”. Asymmetric RSMs are collected over a range of 13.5° in ω-2θ with a step size of 200” and 4.5° in ω with a step size of 250”. Similarly, for the ZrC films, 2θ-ω scans between 25° and 100° are obtained using double-axis diffraction with a step size of 0.05° and a dwell time of 1 s.

2.3.4 Transmission Electron Microscopy

Transmission electron microscopy (TEM) is employed in order to characterize the film microstructure and to determine film thicknesses. Electron-transparent cross-sectional TEM (XTEM) samples are prepared using 30 kV Ga^+ ions in an FEI Nova 600 NanoLab DualBeam^{TM} scanning electron microscopy/focused ion beam (SEM/FIB) milling system. Prior to FIB milling, the film surfaces are protected by a 1-μm-thick layer of carbon deposited using 30 kV and 0.1 nA electron beams. TEM images of the film and the film-substrate interface are acquired using an FEI Titan 80-300 kV S/TEM operated at 300 kV for imaging and selected area electron diffraction (SAED) and at 200 kV for energy dispersive x-ray spectroscopy (EDS). SAED patterns are obtained from the film and substrate as a means to determine the crystallinity of the sample and the film-substrate interface. EDS spectra are collected across the Zr/Al_2O_3 interfaces and ZrC/Al_2O_3 using an Oxford Instruments X-Max^N Silicon Drift Detector with a detection area of 20 mm^2, resolution of 136 eV at 5.9 keV, and bias of -500 V.

Chapter 3: Zr Thin Film Results

3.1 *In situ* Characterization

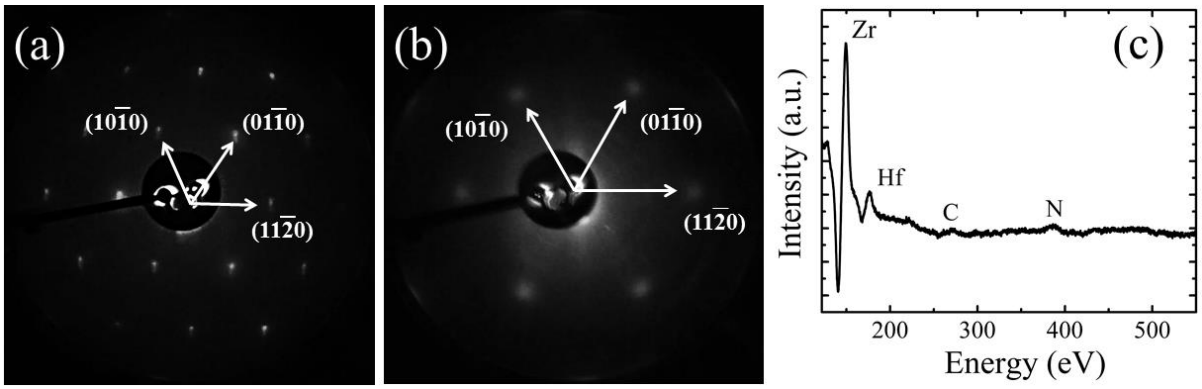

Figure 1: Low energy electron diffraction (LEED) patterns of (a) bare Al_2O_3(0 0 0 1) substrate and (b) Zr thin film sputter-deposited on Al_2O_3(0 0 0 1) at $T_s \approx 700$ °C. (c) AES data obtained from a Zr film, deposited under similar conditions as the sample in (a), show peaks at 145 eV, 172 eV, 270 eV, and 383 eV corresponding to Zr, Hf, C, and N, respectively.

Figures 1(a) and 1(b) are representative LEED patterns acquired *in situ* from a bare Al_2O_3(0 0 0 1) substrate and Zr layer sputter-deposited at $T_s \approx 700$ °C on the *same* Al_2O_3 substrate, respectively. The incident electron energies for both patterns are set to 104 eV. In Fig. 1(a), I observe six-fold symmetric spots characteristic of corundum-structured Al_2O_3(0 0 0 1). The LEED pattern (see Fig. 1(b)) from the Zr film surface is also six-fold symmetric, suggestive of hexagonal structure. Using the LEED spots corresponding to Al_2O_3(0 0 0 1) and assuming an in-plane lattice constant of 0.4759 nm for the substrate,[33] I calibrate the pixels in both the LEED patterns. This allows us to quantitatively index the LEED patterns obtained from the film. From the LEED reflections in Fig. 1(b), I calculate an in-plane lattice parameter of 0.31 ± 0.02 nm. This value is, within experimental uncertainties, in good agreement with the interatomic spacing (0.3223 nm) of (0 0 0 1) surface of bulk Zr.[3, 34] Figure

1(c) is a typical plot of AES data obtained from the Zr/Al_2O_3(0 0 0 1) film. The spectrum shows a peak at 145 eV corresponding to Zr, another peak 172 eV corresponding to Hf,[35, 36] and smaller peaks at 270 eV and 383 eV,[37] likely due to C and N, respectively. I attribute the detection of Hf in my films to Hf impurities present in my Zr sputter target. The origin of C and N peaks in my samples is not clear, but I speculate that they are likely due to cracking of residual gases present in the chamber by the Auger electron gun filament.

3.2 Growth of Single-Crystalline Zr/Al_2O_3(0001)

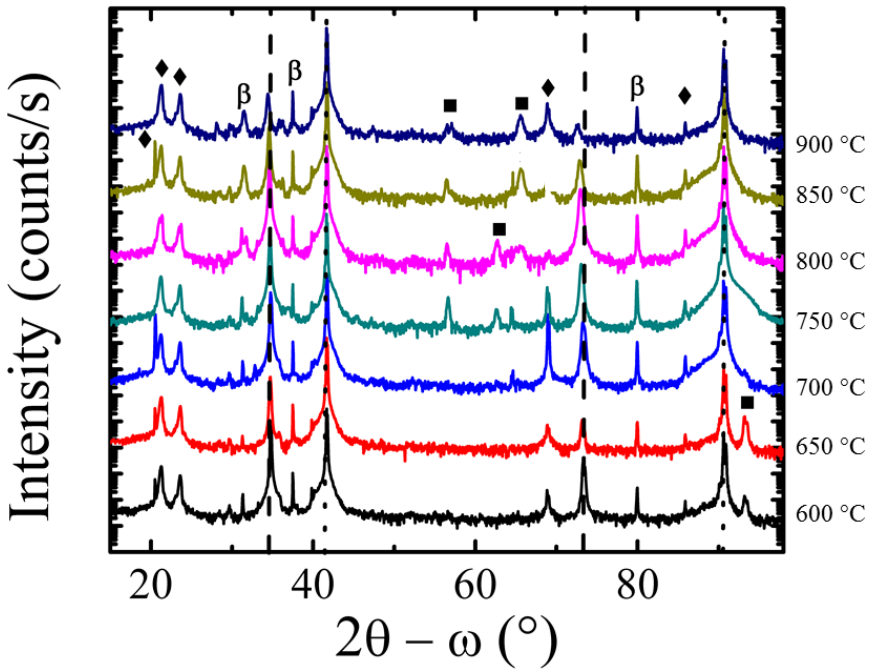

Figure 2: X-ray diffraction (XRD) measurements with intensities given on log scales. 2θ-ω XRD scans from Zr thin films deposited at T_s between 600 and 900 °C. In the plot, the dashed lines correspond to the {0 0 0 2} peaks of the Zr film, the dotted lines denote Al_2O_3 substrate {0 0 0 6} reflections, the symbols ♦ indicate background peaks, ■ correspond to the Zr peaks other than {0 0 0 2} orientation, and β due to Cu K_β wavelength peaks of the film and substrate. There are a few other unidentified low-intensity peaks, some of which could be due to Zr-Al intermetallics.

In order to identify the relationship between Zr film crystallinity and T_s, Zr films are grown at intervals of 50 K between 600 °C and 900 °C. Fig. 2 shows the 2θ-ω scans obtained from these Zr/Al_2O_3(0 0 0 1) samples. The dotted and dashed lines in Fig. 2 correspond to the bulk-relaxed Zr(0 0 0 2), Al_2O_3(0 0 0 6), Zr(0 0 0 4), and Al_2O_3(0 0 0 12) reflections at 2θ values of 34.55°, 41.70°, 73.30°, and 90.90°, respectively[5, 33]. In my data, I observe the higher intensity peaks aligned along these lines. Additional Zr peaks are indicated by solid squares in Fig. 2 and correspond to (1 1 $\bar{2}$ 0), (1 0 $\bar{1}$ 3), (2 0 $\bar{2}$ 0), and (2 1 $\bar{3}$ 0) reflections at 2θ = 56.9 °, 62.9°, 65.8°, and 93.3°, respectively. These peaks are most prevalent in films deposited at $T_s \geq 800$ °C. I speculate that this trend is due to the instability of the hcp lattice as the T_s approaches hcp ↔ bcc transition temperature of 863 °C.[4] As I show below, additional peaks that do not correspond to Zr, Al_2O_3, or known Si background are likely due to Zr-Al intermetallic compounds.

In Fig. 3, I present the results of my highest crystalline quality Zr film. Fig 3(a) is a higher resolution 2θ-ω XRD scan from the Zr film deposited at 700 °C showing peaks due only to Zr(0 0 0 2), Zr(0 0 0 4), the substrate and the background. The absence of additional Zr reflections is suggestive of single-crystalline growth of Zr(0 0 0 1) on Al_2O_3(0 0 0 1). The inset in this plot shows the ω-rocking curve of the Zr (0 0 0 2) peak at 34.55° with a full width half maximum value of ~1°.

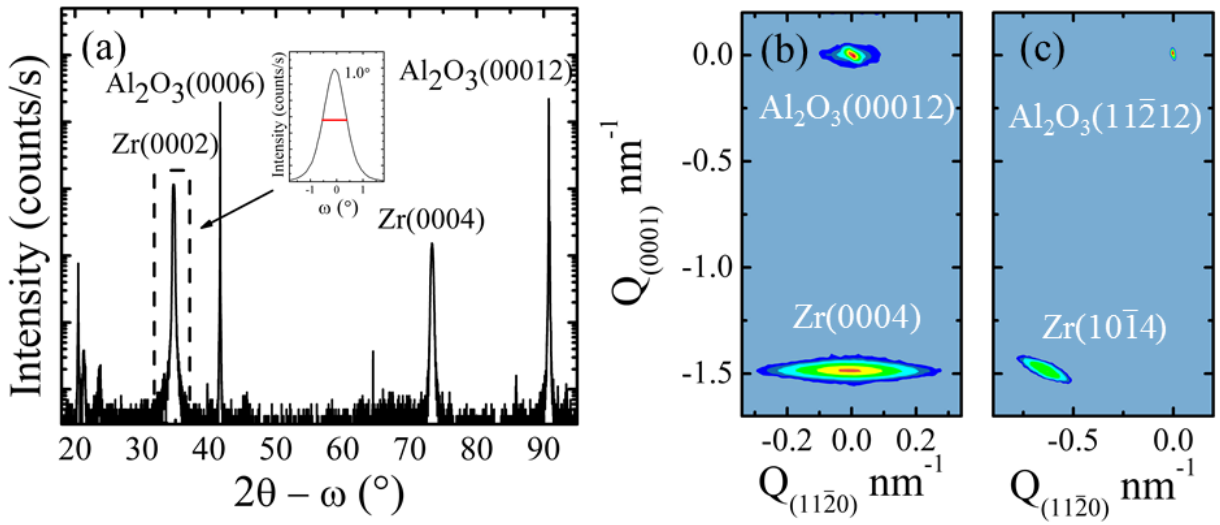

Figure 3: (a) 2θ-ω scan obtained from ~220 nm thick Zr film sputter deposited on Al_2O_3(0 0 0 1) substrate at $T_s \approx$ 700 °C. The higher intensity substrate and film peaks are labeled as shown. The lower intensity peaks at 2θ values below 30° are due to the background. Inset shows the ω-rocking curve for the Zr(0 0 0 2) peak. (b) High-resolution symmetric (0 0 0 12) and (c) asymmetric (1 1 $\bar{2}$ 12) reciprocal space maps obtained from the same sample.

Figures 3(b) and 3(c) are symmetric and asymmetric RSMs of the Al_2O_3(0 0 0 1) substrate and Zr layers acquired around (0 0 0 1) and (1 1 $\bar{2}$ 12), respectively. The axes in the RSM represent the inverse interplanar spacings for both (0 0 0 1) and (1 1 $\bar{2}$ 0) orientations. Thus, I use the known locations of the substrate (0 0 0 12) and (1 1 $\bar{2}$ 12) peaks as reference points. Then measuring the distances of Zr film symmetric and asymmetric peaks from the known substrate peaks at (0,0), I am able to calculate the lattice parameters. From the symmetric RSM, I determine an out-of-plane lattice parameter c = 0.516 ± 0.001 nm. Similarly, from the asymmetric RSM, I measure an a value of 0.324 ± 0.001 nm. In comparison, c = 0.5149 nm and a = 0.3233 nm for bulk Zr.[3] Based upon these results, I conclude that the as-deposited Zr layers are fully relaxed with hexagonal close-packed

structure. From the Zr peak positions in the RSMs, I identify the film-substrate orientation relationships as Zr(0 0 0 4) ‖ Al_2O_3(0 0 0 12) and Zr(1 0 $\bar{1}$ 0) ‖ Al_2O_3(1 1 $\bar{2}$ 0).

3.3 Film-Substrate Interfacial Layer

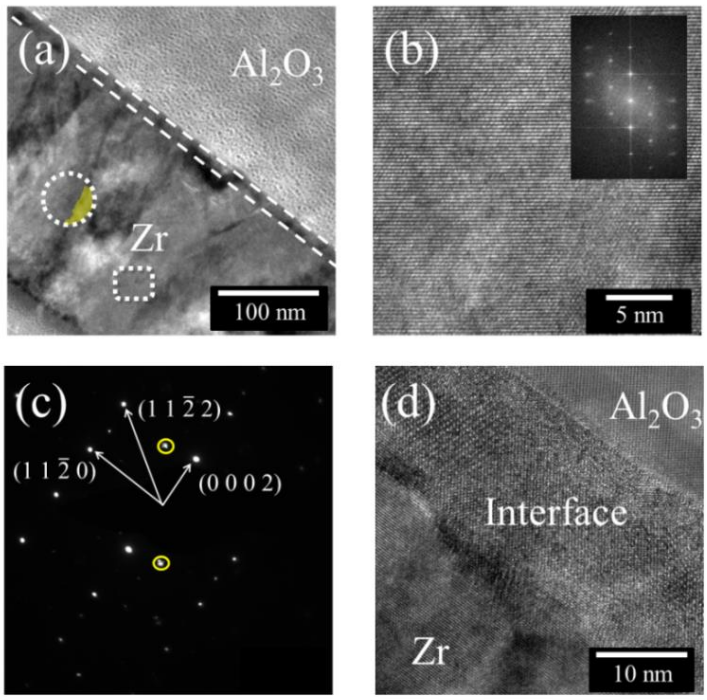

Figure 4: Cross-sectional transmission electron microscopy (XTEM) images acquired from a Zr-Al_2O_3(0 0 0 1) thin film interface in a sample deposited at $T_s \approx 700$ °C. (a) Low magnification XTEM image showing Zr film, interface layer (indicated by dashed white lines), and Al_2O_3 substrate. (b) Higher resolution XTEM image of the Zr film from the region highlighted by the white dotted square in (a). (c) Selected area electron diffraction (SAED) pattern obtained from the circular region within the Zr film, shown in (a). Primary spots are indexed as shown with secondary spots, indicated by the yellow circles, due to an adjacent grain rotated ~36°, highlighted by yellow color within the circular region in (a). (d) Higher magnification XTEM image of the film-substrate interface.

In an effort to better understand the film microstructure and identify the source of the additional peaks observed in Figs. 2 and 3(a), I used TEM. Figs. 4(a) and 4(b) are bright-field

XTEM images acquired from the Zr film-Al_2O_3 substrate interface of the sample grown at T_s ≈ 700 °C. From the low magnification TEM image in Fig. 4(a), it can be seen that the Zr layer exhibits columnar growth with an average column width of ~60 nm. Fig. 4(b) is a higher resolution TEM image obtained from one of the Zr columns highlighted by the dotted square in Fig. 4(a), which shows highly ordered atomic planes, indicative of single-crystallinity. The inset in Fig. 4(b) is a Fourier transform of the image showing single-crystalline reflections corresponding to (1 1 $\bar{2}$ 0), from which I measure the in-plane lattice parameter as 0.30 ± 0.02 nm, consistent with my RSM data. Fig. 4(c) is a SAED pattern obtained from the dotted circular region shown in Fig. 4(a) acquired along [1 $\bar{1}$ 0 0] zone-axis. The spot pattern confirms that the columnar regions in the Zr films are crystalline. The two sets of spots visible in Fig. 4(c) correspond to diffractions from two adjacent grains rotated by ~36° with respect to each other. Fig. 4(d) shows three distinct crystalline regions: the substrate, an interface layer, and the film.

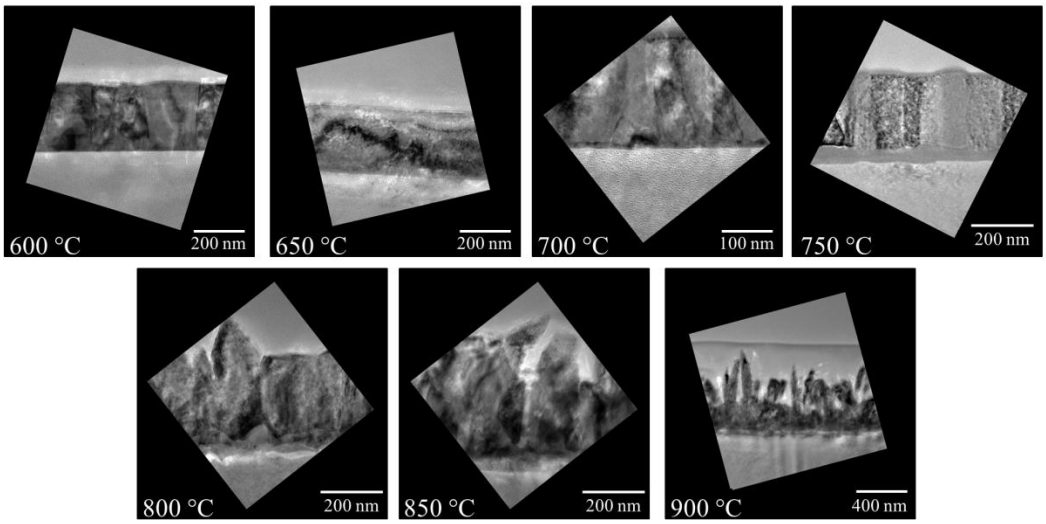

Figure 5: Bright field XTEM images of Zr/Al_2O_3(0 0 0 1) films deposited at different temperatures, T_s.

In order to determine the source and T_s dependence of this interfacial layer, I prepared XTEM samples for all of the films deposited at T_s between 600 °C and 900 °C. Fig. 5 shows

the T_s dependence of film thickness, interface thickness, as well as the surface roughness. Clearly, the interfacial layer thickness is directly dependent on the substrate temperature. At $T_s \approx 600$ °C, I did not observe any interfacial layer. However, TEM imaging may not provide an accurate measure of the thickness of this interfacial layer. Thus, I will present below an alternate approach to measure the thicknesses.

The film surface morphology is also highly dependent on T_s. Notice the development of highly rough and extremely porous morphologies in the films grown at $T_s > 800$ °C. From the XTEM images in Fig. 5, I measure the total film thicknesses which vary between 220 ± 10 nm and 315 ± 20 nm. At $T_s \geq 850$ °C the thickness becomes difficult to quantify due to the porosity of the films.

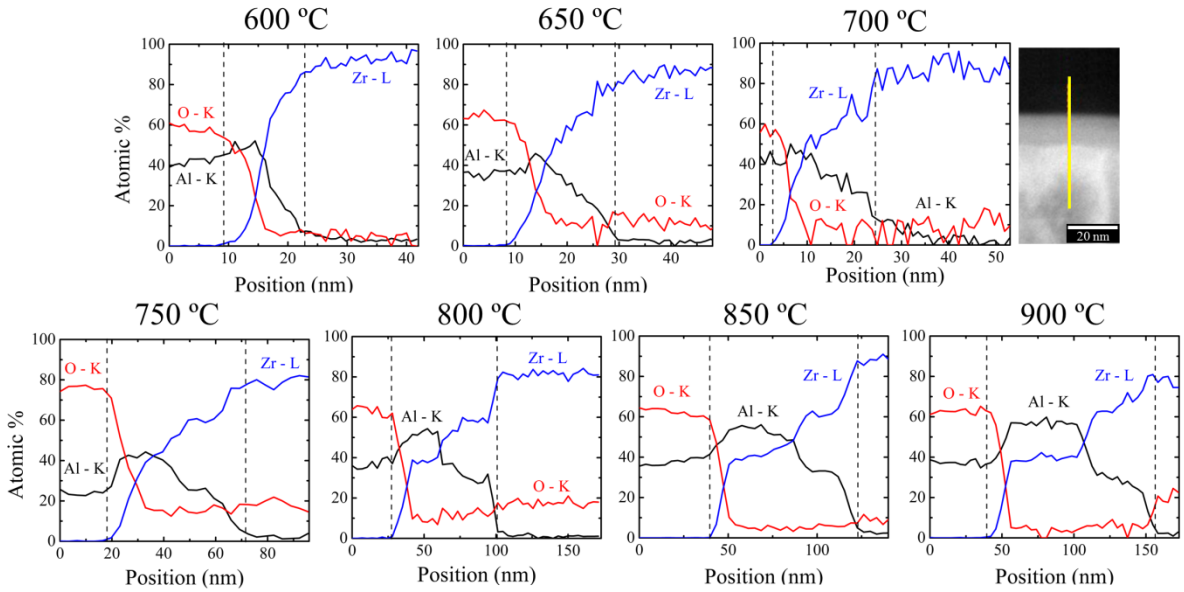

Figure 6: Energy dispersive x-ray spectra (EDS) acquired across the Zr-Al_2O_3(0 0 0 1) interface. Each of the curves, color-coded for clarity, show spatial variations in Zr, Al, and O contents across the film-substrate interface. The interfacial layer is indicated by the region between the dotted lines. The substrate and Zr film are located to the left and right of this region, respectively. A typical scanning TEM image from the 700 °C sample shows the position of the EDS scan with respect to the interface indicated by the yellow line.

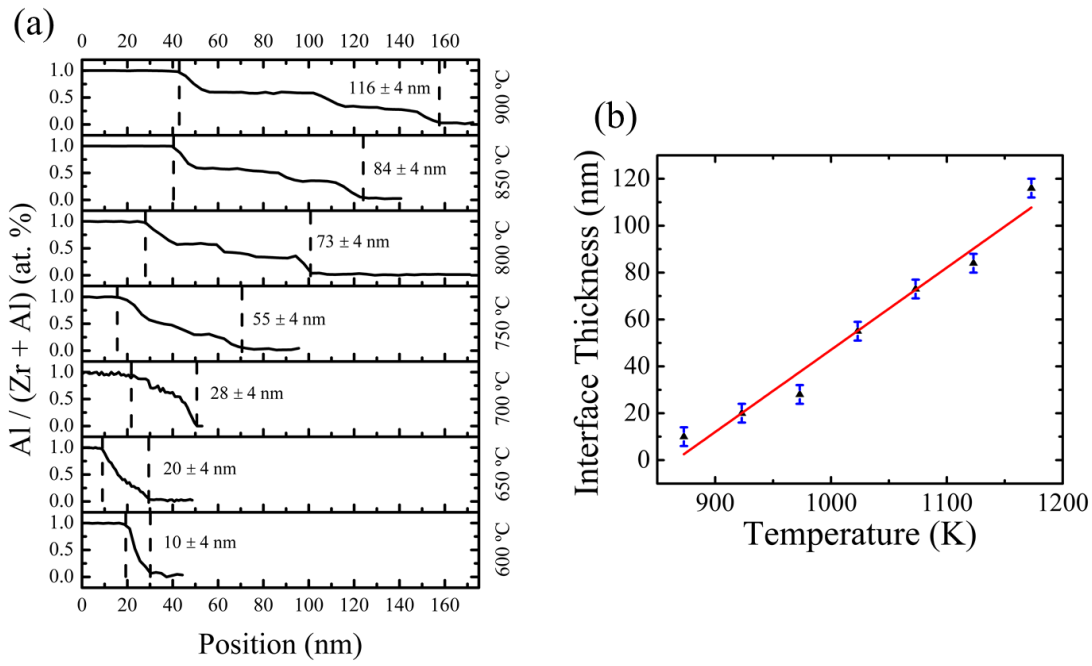

Figure 7: (a) Temperature dependence of Zr-Al interface showing the relative ratio of Al at.% to Zr + Al at.%. Dotted lines indicate the film-substrate interfacial regions. Thicknesses of the interfaces are listed in the plots. (b) Plot of interface thickness as a function of T_s. The solid red line is least-squares linear fit to the data.

The composition of the interfacial layer was determined via EDS, seen in Fig. 6. This data suggests that the interfacial region develops as a result of interdiffusion between Zr and Al from the film and substrate, respectively. The plot in Fig. 6 shows spatial variations in Zr, Al, and O contents across the film-substrate interface. The associated STEM image shows the location of the EDS line scan (yellow line). Primarily Zr is found in the film and both Al and O in the substrate, as expected. I define the boundaries of the interface region based upon the Zr/Al ratios with the onset of the highest and lowest values corresponding to the beginning of the film and substrate regions, respectively. Interestingly, varying concentrations of Zr and Al are observed within the interface. (These results are consistent with previous studies, where similar interfacial reactions have been observed during the deposition of Ti on Al_2O_3.)[38-40] Within the interface, it can be noted that Zr concentration increases while Al content

decreases. The inversely varying concentrations of Zr and Al are suggestive of interdiffusion of Zr and Al during deposition. Interfacial reactions between Zr and Al_2O_3 have also been reported during high-temperature (T > 1000 °C) annealing.[41-43] However, given that my growth temperatures are relatively lower, I speculate that plasma irradiation during the early stages of deposition lead to decomposition of the Al_2O_3 surface to form elemental Al followed by the reaction of Al with the deposited Zr.

In order to identify the mechanisms leading to the formation of the interfacial layer, I investigated the composition of the Zr-Al_2O_3 interfaces in my samples grown at different T_s. I used EDS and acquired line scans across the interfaces. The plots in Fig. 7(a) show the special variations in $\frac{\text{Al}}{\text{Al+Zr}}$ across the interfaces as a function of T_s. The data reveals that the interfacial layer composition and thickness are directly dependent on deposition temperature. The interfacial thickness scales linearly with T_s [see Fig. 7(b)]. I see that at the minimum growth temperature of 600 °C the interfacial layer is practically non-existent. Interestingly, at temperatures above 700 °C, the EDS data exhibit two distinct interfacial regions, where the Zr/Al ratios are constant at 0.6 and 0.33, with higher Zr/Al ratio observed closer to the films. The two likely Zr-Al compounds with such compositions are Zr_2Al_3 and Zr_2Al. From my XRD data, several peaks can be due to either of these compounds and further characterization is necessary to accurately identify the compounds in these regions.

3.4 Outlook

I believe that the presence of this interfacial layer is one cause for the lack of single-crystallinity in my Zr thin films deposited at high temperatures. In addition, I speculate that this interface layer contributes to the increased surface roughness seen in these Zr films. For

these reasons, it is desirable to eliminate this interfacial layer. Both Fig. 2 and Fig. 6 show that the Zr-Al layer is absent in the Zr films deposited at $T_s \approx 600$ °C. However, XRD obtained from the films deposited at 600 °C also reveals the presence of peaks other than {0 0 0 2}, suggestive of polycrystalline Zr growth. Therefore, I am optimistic that single-crystalline Zr thin films with compositionally-abrupt interfaces can be grown on Al_2O_3(0 0 0 1) substrates with careful optimization of the process parameters. One possible approach could be the deposition of an ultra-thin (~2 nm) Zr layer at 600 °C followed by a thicker film at $T_s \approx 700$ ^{o}C.

Chapter 4: ZrC Thin Film Results

4.1 X-ray Diffraction Data

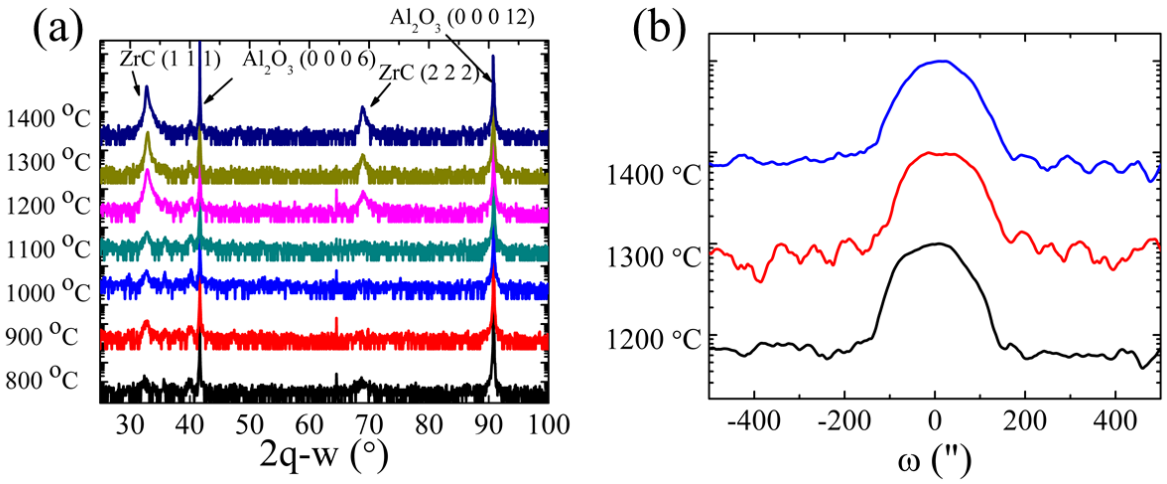

Figure 8: XRD data of ZrC/Al_2O_3(0 0 0 1) thin films grown at various temperatures. (a) 2θ-ω spectra of as-deposited layers as a function of T_s. Single-crystalline ZrC(1 1 1) film peaks are more pronounced in samples deposited at $T_s \geq 1200$ °C. (b) ω-rocking curves obtained from the three films grown at 1200 °C, 1300 °C, and 1400 °C. The full widths at half maxima are approximately the same, ~170" for all these films.

Figure 8(a) is a typical 2θ-ω XRD scan obtained from the ZrC/Al_2O_3 films grown at T_s between 800 and 1400 °C. In all the scans, the Al_2O_3 (0 0 0 6) and (0 0 0 12) substrate peaks are seen at 2θ = 41.68° and 90.78°, respectively. The two additional peaks at 2θ = 32.88° and 68.88°, correspond to ZrC (1 1 1) and (2 2 2), respectively. Please note that these are high resolution XRD scans and hence only those peaks with the highest intensities are visible; the other lower intensity peaks associated with polycrystalline layers are not detected. In order to further quantify the quality of the ZrC films, ω-rocking curves were collected around the ZrC(1 1 1) peak from the films deposited at $T_s \geq 1200$ °C films. The data presented in Fig. 8(b) reveal full width-half maxima values of ~170" for all three films. This result suggests

that the crystallinity of ZrC films deposited at T_s > 1200 °C is independent of T_s. However, as I will show below the film composition is sensitive to T_s.

4.2 X-ray Photoelectron Spectroscopy of ZrC Thin Films

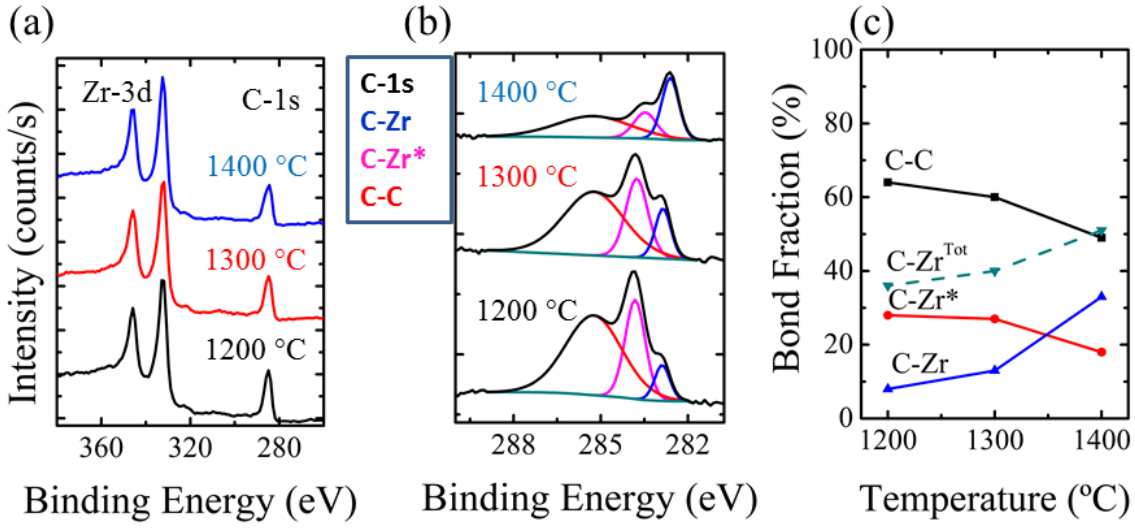

Figure 9: (a) X-ray photoelectron spectra (XPS) of the Zr-3d and C-1s peaks of ZrC/Al_2O_3(0 0 0 1) thin films deposited at of 1200 °C, 1300 °C, and 1400 °C. (b) High resolution XPS data of the C-1s peaks fit with three peaks corresponding to C-C, C-Zr*, and C-Zr bonds. (c) Plot of relative fractions of the three bonding types and total C-Zr bonding vs. T_s.

XPS data were obtained from ZrC samples grown at $T_s \approx 1200 – 1400$ °C. The XPS survey in Fig. 9(a) shows two sets of peaks, two peaks corresponding to Zr-3d around 340 eV and one C-1s peak around 280 eV. From the peak intensities, I estimate that the Zr and C contents in the films are 40 at.% and 60 at.%, respectively. In order to distinguish the relative fractions of free carbon and carbon bonded to Zr, I acquired high-resolution XPS data around the C-1s peak (see Fig. 9(b)) from ZrC samples grown at $T_s \geq 1200$ °C. The three peaks present within all the three scans are the C-C (284.8 eV), C-Zr* (283.0 eV), and C-Zr (282.1 eV). Both the C-Zr* and C-Zr peaks are associated with bonded C while the C-C bonds are due to free

carbon.[44, 45] Based upon the relative intensities of the peaks and the areas under the peaks, I estimate the total amount of carbon in the ZrC matrix to be 22% at 1200 °C, 24% at 1300 °C, and 28% at 1400 °C. That is, the amount of bonded C increases and the amount of free carbon decreases with increasing T_s. However, additional characterization is necessary to determine the stoichiometry of my ZrC films.

4.3 Microstructure

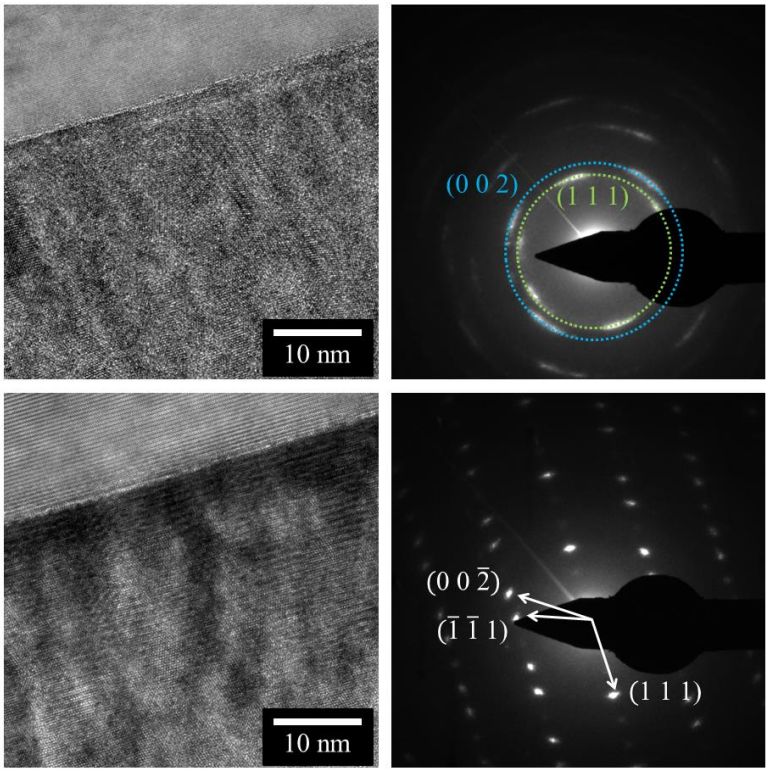

Figure 10: XTEM images and SAED patterns obtained from ZrC/Al_2O_3(0 0 0 1) thin films deposited at $T_s \approx$ (top panel) 1100 °C and (bottom panel) 1400 °C.

The top and bottom panels in Fig. 10 show XTEM images and SAED patterns acquired from around the ZrC film-Al_2O_3 substrate interfaces in samples grown at $T_s \approx$ 1100 °C and 1400 °C, respectively. These particular samples are selected in order to compare and contrast the microstructures of polycrystalline (i.e., $T_s \approx$ 1100 °C) and single-crystalline (i.e., $T_s \approx$ 1400

°C) ZrC films. From the XTEM images, I determine the film thicknesses as ~110 nm and ~40 nm in samples deposited at $T_s \approx 1100$ °C and 1400 °C, respectively. At lower T_s, the films lack the highly ordered atomic planes. The associated SAED pattern is indicative of texture, i.e., preferred orientation. Based upon this data, I conclude that the ZrC films sputter-deposited at $T_s \leq 1100$ °C are polycrystalline and exhibit texture. With increasing $T_s \geq 1200$ °C, I obtain highly 111-oriented ZrC films. For example, the lower panel in Fig. 10 shows the XTEM image obtained from the sample grown at $T_s \approx 1400$ °C. The highly periodic pattern observed in the image is suggestive of single-crystallinity. The associated SAED pattern further supports my conclusion.

Chapter 5: Conclusions

In conclusion, I was able to grow single-crystalline zirconium and zirconium carbide thin films on Al_2O_3(0 0 0 1) substrates via dc magnetron sputtering in an ultra-high vacuum system. I observed that for Zr films, deposition at 700 °C produced single-crystalline films, but as the growth temperature increases towards that of the transition temperature from hcp to bcc (863 °C), the films become polycrystalline. In addition, at all growth temperatures at or above 650 °C, an intermetallic Zr-Al forms at the film-substrate interface. This interfacial layer thickness increases with increasing substrate temperature. Based upon my results, I suggest that single-crystalline Zr(0 0 0 2) films with compositionally-abrupt interfaces can be deposited by careful control over the deposition temperature.

In my ZrC growth experiments, I obtain highly-crystalline films at temperatures above 1200 °C and textured polycrystalline layers at lower temperatures. X-ray photoelectron spectra revealed the presence of excess carbon in all of my films with significant amount of free carbon. However, the amount of free carbon decreased while the total amount of C and Zr bonds increased with increasing deposition temperature. In my experiments, the highest quality film, as indicated by the x-ray diffraction data, was grown at a substrate temperature of 1400 °C. I would also like to point out that irrespective of the deposition temperatures, I did not observe any interfacial reactions between the film and the substrate.

Future plans for this study involve the elimination of the Zr-Al interfacial layer for higher deposition temperatures. One potential approach is to grow an ultra-thin Zr layer at 600 °C, then deposit a thicker Zr film at the higher temperature. Another method for increasing the quality of the ZrC thin films is to identify the growth conditions for the deposition of

stoichiometric films. This could be done by changing the partial pressures of the reactive ethylene gas in the deposition atmosphere. A future use for Zr films is to be used as a source for the growth of ZrC layers. Thus, the kinetics of carburization of these films needs to be investigated. Finally, nano-mechanical properties of ZrC thin films as a function of film composition and crystallinity could be investigate.

References

[1]R. Raj, Journal of the American Ceramic Society **76** (9), 2147-2174 (1993).

[2]L. E. Toth, *Refractory Materials*. (Academic Press, New York, 1971).

[3]J. Goldak, L. T. Lloyd and C. S. Barrett, Physical Review **144** (2), 478-484 (1966).

[4]T. Wang, Z. Jin and J.-C. Zhao, Journal of Phase Equilibria **22** (5), 544-551 (2001).

[5]R. H. Nielsen and G. Wilfing, in *Ulmann's Encyclopedia of Industrial Chemistry* (Wiley-VCH, 2010).

[6]B. Lustman and F. Kerze Jr., *Metallurgy of Zirconium*. (McGraw-Hill Book Company, New York, 1955).

[7]A. Fernández Guillermet, Journal of Alloys and Compounds **217** (1), 69-89 (1995).

[8]*NASA Chemical Reactions of Carbides, Nitrides, and Diborides of Titanium and Zirconium and Chemical Bonding in These Compounds*, Technical Note

[9]Y. S. Won, V. G. Varanasi, O. Kryliouk, T. J. Anderson, L. McElwee-White and R. J. Perez, Journal of Crystal Growth **307** (2), 302-308 (2007).

[10]D. Kim, M. J. Ko, J. Y. Park, M. S. Cho and W.-J. Kim, Journal of Nuclear Materials **451** (1-3), 97-103 (2014).

[11]W. A. Mackie, T. Xie and P. R. Davis, Journal of Vacuum Science & Technology B: Microelectronics and Nanometer Structures **17** (2), 613 (1999).

[12]C. P. Kempter and R. J. Fries, Analytical Chemistry **32** (4), 570-570 (1960).

[13]L. Xu, Y. Xiao, A. van Sandwijk, Q. Xu and Y. Yang, Journal of Nuclear Materials **466**, 21-28 (2015).

[14]S. C. Lumley, S. T. Murphy, P. A. Burr, R. W. Grimes, P. R. Chard-Tuckey and M. R. Wenman, Journal of Nuclear Materials **437** (1-3), 122-129 (2013).

[15]A. Singh, N. Kumar, P. Kuppusami, T. N. Prasanthi, P. Chandramohan, S. Dash, M. P. Srinivasan, E. Mohandas and A. K. Tyagi, Wear **280-281**, 22-27 (2012).

[16]L. Mercatelli, E. Sani, D. Jafrancesco, P. Sansoni, D. Fontani, M. Meucci, S. Coraggia, L. Marconi, J. L. Sans, E. Beche, L. Silvestroni and D. Sciti, Energy Procedia **49**, 468-477 (2014).

[17]E. G. Njoroge, C. C. Theron, J. B. Malherbe and O. M. Ndwandwe, Nuclear Instruments and Methods in Physics Research Section B: Beam Interactions with Materials and Atoms **332**, 138-142 (2014).

[18]K. Benouareth, P. Tristant, C. Jaoul, C. Le Niniven, C. Nouveau, C. Dublanche-Tixier and A. Bouabellou, Vacuum **125**, 234-239 (2016).

[19]W. Liu, C. Wen, Q. Liu, L. Mao, X. Zhou, X. Long and S. Peng, Journal of Nuclear Materials **461**, 325-328 (2015).

[20]P. Sarin, P. E. Driemeyer, R. P. Haggerty, D. K. Kim, J. L. Bell, Z. D. Apostolov and W. M. Kriven, Journal of the European Ceramic Society **30** (11), 2375-2386 (2010).

[21]Q. N. Meng, M. Wen, F. Mao, N. Nedfors, U. Jansson and W. T. Zheng, Surface and Coatings Technology **232**, 876-883 (2013).

[22]V. C. Gudla, K. Bordo, S. Engberg, K. Rechendorff and R. Ambat, Materials & Design **95**, 340-347 (2016).

[23]W. Liu, J. Liang, X. Zhou and X. Long, Materials Letters **122**, 220-222 (2014).

[24]Y. Zhu, M. Ikeda, Y. Murakami, A. *T*sukazaki, T. Fukumura and M. Kawasaki, Jpn. J. Appl. Phys. Part 2 - Lett. Express Lett. **46** (41-44), L1000-L1002 (2007).

[25]T. C. Tessner and P. R. Davis, Journal of Vacuum Science & Technology A **11** (1), 1-5 (1993).

[26]J. Woo, Dissertation, The University of Florida, 2005.

[27]D. Craciun, G. Socol, E. Lambers, E. J. McCumiskey, C. R. Taylor, C. Martin, N. Argibay, D. B. Tanner and V. Craciun, Applied Surface Science **352**, 28-32 (2015).

[28]M. Yoshitake, T. Nosaka, A. Okamoto, S. Ogawa and K. Nishikawa, Thin Solid Films **221** (1), 72-78 (1992).

[29]J. Brückner and T. Mäntylä, Surface and Coatings Technology **59** (1), 166-170 (1993).

[30]C.-S. Chen and C.-P. Liu, Journal of Electronic Materials **34** (11), 1408-1413 (2005).

[31]M.-h. Ding, H.-S. Zhang, C. Zhang and X. Jin, Surface and Coatings Technology **224**, 34-41 (2013).

[32]*Omega Transactions in Measurement and Control*, Technical Reference

[33]E. R. Dobrovinskaya, L. A. Lytvynov and V. Pishchik, 55-176 (2009).

[34]W. Bond, Acta Crystallographica **13** (10), 814-818 (1960).

[35]M. Y. Zhou, R. H. Milne, M. A. Karolewski, D. C. Frost and K. A. R. Mitchell, Surface Science Letters **139** (1), L181-L184 (1984).

[36]M. F. Chung and L. H. Jenkins, Surf. Sci. **22** (2), 479-& (1970).

[37]D. Briggs and M. P. Seah, *Auger and X-ray Photoelectron Spectroscopy*. (John Wiley & Sons, New York, 1990).

[38]O. Wilhelmsson, J. P. Palmquist, E. Lewin, J. Emmerlich, P. Eklund, P. O. Å. Persson, H. Högberg, S. Li, R. Ahuja, O. Eriksson, L. Hultman and U. Jansson, Journal of Crystal Growth **291** (1), 290-300 (2006).

[39]P. O. Å. Persson, S. Kodambaka, I. Petrov and L. Hultman, Acta Materialia **55** (13), 4401-4407 (2007).

[40]A. M. Kliauga and M. Ferrante, Journal of Materials Science **35** (17), 4243-4249 (2000).

[41]R. E. Loehman, F. M. Hosking, B. Gauntt, P. G. Kotula and P. Lu, Journal of Materials Science **40** (9), 2319-2324 (2005).

[42]R. E. Loehman and A. P. Tomsia, Acta Metallurgica et Materialia **40**, S75-S83 (1992).

[43]X. A. Zhao, E. Kolawa and M. A. Nicolet, Journal of Vacuum Science & Technology A **4** (6), 3139-3141 (1986).

[44]M. Andersson, S. Urbonaite, E. Lewin and U. Jansson, Thin Solid Films **520** (20), 6375-6381 (2012).

[45]A. Escudeiro, N. M. Figueiredo, T. Polcar and A. Cavaleiro, Applied Surface Science **325**, 64-72 (2015).